Novel phase of carbon, ferromagnetism, and conversion into diamond

Jagdish Narayan and Anagh Bhaumik

Citation: Journal of Applied Physics **118**, 215303 (2015); doi: 10.1063/1.4936595
View online: http://dx.doi.org/10.1063/1.4936595
View Table of Contents: http://scitation.aip.org/content/aip/journal/jap/118/21?ver=pdfcov
Published by the AIP Publishing

JOURNAL OF APPLIED PHYSICS **118**, 215303 (2015)

Novel phase of carbon, ferromagnetism, and conversion into diamond

Jagdish Narayan[a] and Anagh Bhaumik
Department of Materials Science and Engineering, Centennial Campus, North Carolina State University, Raleigh, North Carolina 27695-7907, USA

(Received 16 September 2015; accepted 10 November 2015; published online 2 December 2015)

We report the discovery of a new phase of carbon (referred to as Q-carbon) and address fundamental issues related to direct conversion of carbon into diamond at ambient temperatures and pressures in air without any need for catalyst and presence of hydrogen. The Q-carbon is formed as result of quenching from super undercooled state by using high-power nanosecond laser pulses. We discuss the equilibrium phase diagram (P vs. T) of carbon and show that by rapid quenching kinetics can shift thermodynamic graphite/diamond/liquid carbon triple point from 5000 K/12 GPa to super undercooled carbon at atmospheric pressure in air. It is shown that nanosecond laser heating of diamond-like amorphous carbon on sapphire, glass, and polymer substrates can be confined to melt carbon in a super undercooled state. By quenching the carbon from the super undercooled state, we have created a new state of carbon (Q-carbon) from which nanodiamond, microdiamond, microneedles, and single-crystal thin films are formed depending upon the nucleation and growth times allowed for diamond formation. The Q-carbon quenched from liquid is a new state of solid carbon with a higher mass density than amorphous carbon and a mixture of mostly fourfold sp^3 (75%–85%) with the rest being threefold sp^2 bonded carbon (with distinct entropy). It is expected to have new and improved mechanical hardness, electrical conductivity, chemical, and physical properties, including room-temperature ferromagnetism (RTFM) and enhanced field emission. Here we present interesting results on RTFM, enhanced electrical conductivity and surface potential of Q-carbon to emphasize its unique properties. The Q-carbon exhibits robust bulk ferromagnetism with estimated Curie temperature of about 500 K and saturation magnetization value of 20 emu g^{-1}. From the Q-carbon, diamond phase is nucleated and a variety of micro- and nanostructures and large-area single-crystal diamond sheets are grown by allowing growth times as needed. Subsequent laser pulses can be used to grow nanodiamond into microdiamond and nucleate other nanostructures of diamond on the top of existing microdiamond and create novel nanostructured materials. The microstructural details provide insights into the mechanism of formation of nanodiamond, microdiamond, nanoneedles, microneedles, and single-crystal thin films. This process allows carbon-to-diamond conversion and formation of useful nanostructures and microstructures at ambient temperatures in air at atmospheric pressure on practical and heat-sensitive substrates in a controlled way without need for any catalysts and hydrogen to stabilize sp^3 bonding for diamond formation. © *2015 AIP Publishing LLC*. [http://dx.doi.org/10.1063/1.4936595]

INTRODUCTION

Direct conversion of carbon into diamond at ambient pressures and lower temperatures is scientifically challenging with immense technological significance.[1–3] Conversion of carbon, one of the most abundant materials in the Earth's crust, into most precious material diamond has been a cherished goal of the scientists all over the world for a long time. Diamond is one of the most desirable materials with many applications ranging from abrasives, protective coatings, and biomedical applications to superior diamond electronics, photonics, and display devices. Conventional bulk processing involves high pressures and temperatures,[1] and chemical vapor deposition (CVD) for thin films requires high temperatures in the presence of hydrogen.[4] These requirements lead to low production volumes and high costs. More recently, another approach for formation of nanodiamond from SiC has been reported at temperatures ~1000 °C under flowing hydrogen and chlorine gases at ambient pressures.[5] Here we show that a direct conversion of carbon into diamond can occur in air at ambient temperatures and pressures without any need for catalysts and hydrogen to stabilize sp^3 diamond bonding. In addition, ferromagnetism in bulk carbon represents another scientific challenge with profound impact on magnetic storage, sensors, data processing, and biomedical applications. These two challenging problems are solved by the discovery of a new state of carbon, referred to as Q-carbon hereafter. In addition, the Q-carbon exhibits enhanced electrical conductivity (of semiconducting and metallic nature), enhanced field emission, and super high hardness. The Q-carbon is formed as result of quenching of super undercooled liquid carbon at the atmospheric pressure that is found to be magnetic, and it plays a critical role in diamond formation. It has been conjectured that liquid carbon may exist as a thermodynamically stable phase at high pressures and temperatures near the cores of Uranus and Neptune planets and contribute to their magnetism.[1] Thus our finding can also explain ferromagnetism in our planetary system and

[a]Author to whom correspondence should be addressed. Electronic mail: narayan@ncsu.edu

formation of natural diamonds among other things. According to the equilibrium (P vs. T) phase diagram (Figure 1),[1] graphite, diamond, liquid, and vapor are thermodynamically stable forms of carbon. At low pressures, graphite converts into vapor above around 4000 K. According to the phase diagram, diamond synthesis from liquid carbon will require even higher temperatures and pressures as the graphite/diamond/liquid carbon triple point occurs at 5000 K/12 GPa, where 1 GPa = 9869 atm. Currently, diamond powders are synthesized by graphite to diamond conversion at high pressures and temperatures. Graphite can be transformed into diamond above about 2000 K at 6–10 GPa using a liquid metal (iron) catalyst that is used for commercial synthesis of diamond (Figure 1).[1]

In the thermodynamically stable forms of carbon, graphite, diamond, liquid, and vapor, we introduce amorphous amorphous carbon with some sp^3 content and super undercooled state of liquid carbon (Figure 1).[1] This can be accomplished by nanosecond laser melting of amorphous carbon, where undercooled state is at about 4000 K, some 1000 K below the melting point of graphite.[6] The dotted extension to 4000 K in the phase diagram from the liquid-diamond-graphite triple point at 5000 K represents this super undercooled state, which upon quenching results in the formation of Q-carbon at a temperature slightly lower than 4000 K. Because the molten state of carbon is found to be metallic,[1] the carbon atoms can be fully packed with mass density and hardness exceeding those of diamond. By quenching this super undercooled state, we are able to form Q-carbon, from which nanodiamonds, microdiamonds, and thin films are formed depending upon allowed nucleation and growth times. The new state of carbon (Q-carbon) has a very high fraction of sp^3 bonded carbon, remainder of which is sp^2, and is expected to possess novel physical, chemical, mechanical, and catalytic properties. There is a considerable reduction in volume when as-deposited amorphous carbon is melted in the undercooled state and quenched as Q-carbon. Most interesting of all is that Q-carbon exhibits ferromagnetism at and above room temperature. The formation of cubic diamond phase can occur if a sufficient time is allowed for homogeneous nucleation from the Q-carbon. The substrates which are lattice or planar matched with cubic diamond such as copper and sapphire, aid the epitaxial nucleation of diamond.[2,3]

The phenomenon of undercooling has been studied extensively in the context of solidification kinetics and control of microstructures and properties.[7–12] It became one of the hottest topics in the early MRS meetings[13–15] in the context of pulsed laser annealing,[16] doping, and formation of supersaturated alloys of silicon and germanium.[17] The undercooling in silicon and germanium was estimated to be as high as 241 K and 336 K,[14] respectively. By scaling with graphite melting, the undercooling for amorphous carbon is estimated to be as high as 1000 K. By using nanosecond laser pulses, the formation of nanocrystalline and microcrystalline regions were studied in detail as a function of pulse energy density in doped and undoped amorphous silicon produced by ion implantation.[8,9] The crystallite size and impurity distribution in implanted silicon provided information on mechanism of crystallization and the details of undercooling phenomena. Time-resolved reflectivity measurements of melting and undercooling phenomena in amorphous silicon were correlated with detailed crystallite nucleation, resulting microstructures and modeling calculations.[10,11] The undercooling phenomenon in crystalline carbon was not followed with any vigor due to our understanding from the equilibrium phase diagram, according to which graphite converts into vapor above around 4000 K at low pressures.[1]

The primary focus of this paper is on nanosecond laser melting of amorphous carbon films with sp^3 fraction 20%–50% on sapphire, glass, and polymer substrates. The irradiation of these films with ArF Excimer laser pulses (wavelength 193 nm or photon energy of 6 eV and pulse duration of 20 ns) leads to confinement of laser energy and selective melting of amorphous carbon films. These undercooling values for amorphous carbon are considerably higher than those achieved during melting of crystalline carbon such as HOPG samples, which did not lead to diamond formation. Our results show that under nanosecond pulsed laser melting, amorphous carbon can lead to a highly undercooled state that can be quenched into a new state of Q-carbon from which nanodiamonds, microdiamonds, and thin films are formed. We are also able to create nano- and microneedles, which stand to make a profound impact on biomedical applications. The Q-carbon also exhibits novel properties, including room-temperature ferromagnetism (RTFM) and enhanced hardness and field emission. It should be emphasized that the presence of similar sp^3 fraction in as-deposited amorphous carbon films does not result in RTFM. The nanodiamonds nucleate from the undercooled state, providing a seed for microdiamond formation.

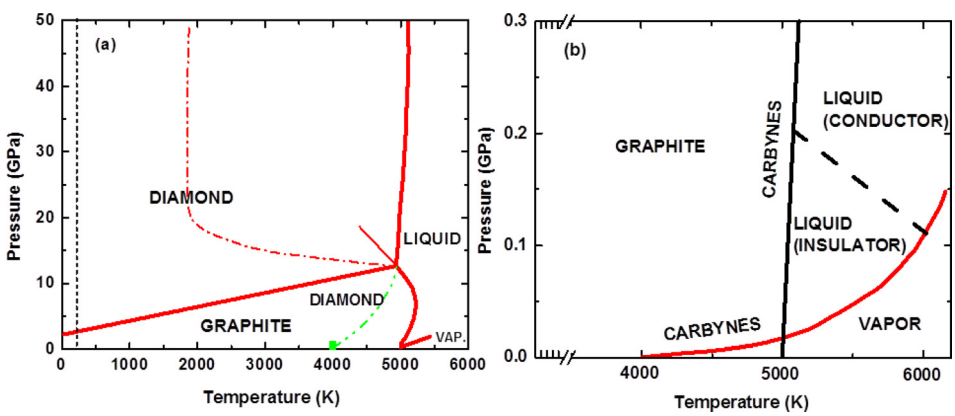

FIG. 1. (a) Carbon phase diagram (P vs. T) following Bundy *et al.*[1] that has amorphous diamond-like carbon melting at 4000 K at ambient pressures (dotted green line) and (b) phase diagram at lower pressures and temperatures.

EXPERIMENTAL

The amorphous carbon films were deposited on sapphire (c-plane), glass, and high-density polyethylene (HDPE) substrates by using KrF laser (pulse duration = 25 ns, wavelength = 248 nm, energy density = 3.0 J cm^{-2}) to a thickness of 50–500 nm. These films were characterized by transmission electron microscopy (TEM) and Raman and found to be amorphous containing Raman signature on sapphire (diamondlike carbon (DLC) broad peak = 1580 cm^{-1}) with estimated sp^3 fraction up to 50%. The Raman spectra for films on glass substrates, contained D (1349 cm^{-1}) and G (1580 cm^{-1}) peaks with considerably less sp^3 around 20%–25%. These films were irradiated in air with ArF laser pulses (Pulse duration = 20 ns, wavelength = 193 nm, energy density = 0.3–0.6 J cm^{-2}). A HORIBA LabRAM ARAMIS superior confocal Raman spectroscope with a lateral resolution less than 200 nm was employed to characterize the Raman active vibrational modes in the as-deposited and laser annealed films. The wavelength of the excitation laser source used was 633 nm. Crystalline Si, which has its characteristic Raman peak at 520.6 cm^{-1}, was used for calibrating the Raman spectroscopy. After the laser treatment, these films were characterized by high-resolution scanning electron microscopy (SEM), electron backscattered diffraction (EBSD) with characteristic diamond Kikuchi patterns, high-resolution TEM (HRTEM) and electron energy loss spectroscopy (EELS), x-ray diffraction, and Raman spectroscopy. High-resolution SEM and EBSD measurements were carried out using FEI Verios 460L SEM and FEI Quanta 3D FEG FIB-SEM for phase identification and determination of grain orientation. Aberration-corrected STEM-FEI Titan 80–300 and JEOL-2010 STEM/TEM were used EELS with resolution of 0.15 eV and high resolution TEM (point-to-point TEM resolution, 0.18 nm; STEM-Z resolution, 0.08 nm with information limit of 0.06 nm). Magnetic measurements were performed in magnetic fields up to 1 T in an Ever Cool Quantum Design physical-property measurements system (PPMS) with a base temperature as low as 10 K. An Asylum Research MFP-3D Infinity AFM was employed for magnetic force microscopy (MFM) and Kelvin-probe force microscopy (KPFM) imaging. Using KPFM, work function of the surface can be obtained with atomic-scale resolution. MFM silicon probe with 50 nm Co-Cr coated tip was used for the MFM scans. The MFM image was taken with a delta height of 50 nm and was flattened to zeroth order to improve its contrast, and results compared with electrostatic force microscopy (EFM) with Pt/Ti cantilever and KPMF work function (surface potential) measurements. The EFM measures electric field gradient distribution through electronic interaction between the conductive tip and the sample surface.

RESULTS AND DISCUSSION

Modified carbon phase diagram

According to the equilibrium (P vs. T) phase diagram,[1] graphite, diamond, liquid, and vapor are thermodynamically stable forms of carbon (Fig. 1(a)). At low pressures, graphite converts into vapor above around 4000 K as shown in Fig. 1(b). According to the phase diagram, diamond synthesis from liquid carbon will require even higher temperatures and pressures as the graphite/diamond/liquid carbon triple point occurs at 5000 K/12 GPa. Consistent with the phase diagram, diamond can exist in the interiors of the outer planets (Uranus and Neptune) and Earth's mantle, where pressure/temperature are 600 GPa/7000 K and 135 GPa/3500 K, respectively. Because of the high binding and activation energy of transformation, carbon polymorphs can exist metastably well into a P-T region, where a different phase is thermodynamically stable. As an example, diamond survives indefinitely at room temperature where graphite is the stable form.

In the thermodynamically stable forms of carbon, graphite, diamond, liquid, and vapor, we introduce amorphous carbon with some sp^3 content and super undercooled state of liquid carbon. This can be accomplished by nanosecond laser melting of amorphous carbon, where undercooled state is at about 4000 K or lower, some 1000 K below the melting point of graphite. This temperature is estimated from model calculations by using Singh and Narayan (SLIM) code.[6] By quenching this super undercooled state, we are able to form nanodiamond, microdiamond, and thin films by controlling the nucleation and growth times and the growth template. The super undercooled state upon rapid quenching leads to formation of new state of carbon (Q-carbon) with novel physical, chemical, mechanical and catalytic properties.

Our results clearly show that diamond can be formed at ambient pressure in air from super undercooled state of carbon, produced by nanosecond pulsed laser melting of amorphous carbon. Thus amorphous state of carbon, laser parameters, and film substrate determine the temperature distribution and undercooling and play a critical role in the nucleation and growth of diamond.[6] By scaling with the melting point of carbon, we estimate the undercooling in carbon to be as high as 1000 K. This undercooling shifts amorphous carbon/diamond/liquid carbon triple point to 4000 K or lower at ambient pressures. This is rather a drastic change from graphite/diamond/liquid carbon triple point at 5000 K/12 GPa in the equilibrium phase diagram in Fig. 1. This shift of amorphous carbon/diamond/liquid carbon triple point to 4000 K or lower at ambient pressures leads to modification[3] of equilibrium carbon phase diagram by Bundy *et al.*[1] to accommodate diamond processing under super undercooled state of carbon. At these transition temperatures, Gibbs free energy of highly undercooled liquid equals that of metastable diamond phase, which is quenched and retained at room temperature.

This transformation from super undercooled state of carbon into diamond, which can occur at 4000 K and ambient pressures, modifies the equilibrium carbon phase diagram as shown in Fig. 1. The extension of the phase diagram (P vs. T) is based upon Simon equation, where $P = P_0 + a[(T/T_r)^c - 1]$, where we used $P_0 = 10^{-4}$ GPa at $T_r = 4000$ K from our experiments and the experimental data of Bundy *et al.*[1] to estimate a and c parameters. From the Simon equation, $(dP/dT)_{Tr} = ac/T_r$ was determined, and the results compared with the value estimated from Clausius-Clapeyron equation,

where $(dP/dT)_{Tr} = \Delta H_m/(T_r \Delta V)$, where ΔV is the change in volume from super undercooled carbon into diamond.[3]

Formation of quenched-in (Q) carbon and diamond

The super undercooled carbon layer is formed near the film-substrate interface, which can break into a cellular (filamentary) structure upon quenching leading to formation of a new state of carbon. The formation of a cellular structure results from interfacial instability at the solid-liquid interface, driven by either by solute segregation or strain.[18] Figure 2(a) shows a cellular structure (SEM micrograph) of Q-carbon filaments (200–500 nm across) formed after laser irradiation with 0.5 J cm^{-2} pulse of the ArF laser. A similar microstructure of filaments was observed in the outer regions of 0.6 J cm^{-2} pulse. This new state quenched from super undercooled carbon, referred as Q-carbon hereafter, has a matrix of mostly sp^3 bonded (>75%) amorphous carbon in which nanocrystallites of diamond are embedded as shown later. As measured by the AFM step shrinkage, the Q-carbon is considerably denser having shorter C-C bond length than amorphous carbon. The number density of diamond nanocrystallites depends upon the time available for crystal growth before quenching. Figure 2(b) illustrates the growth of microdiamonds from the Q-carbon filament, which contained nanodiamond nuclei. Areas in the middle of the 0.6 J cm^{-2} laser irradiated sample contained a high density of nanodiamonds (10–20 nm) and microdiamonds (500–600 nm), as shown in Figure 2(c), and mostly microdiamonds, in Figure 2(d), in certain areas. Thus a direct conversion of carbon into diamond is accomplished by quenching of super undercooled carbon into Q-carbon from which nanodiamonds and microdiamonds can be formed.

When the filaments of Q-carbon are irradiated with a second laser pulse at 0.6 J cm^{-2}, we find interesting details about diamond nucleation and growth. Figure 3(a) shows that Q-carbon filaments turn into microdiamond (average size 250 nm) through the growth of nanodiamonds, some of which preexisted during irradiation with the first pulse. At a higher magnification, we see the details of nanodiamond formation by homogeneous nucleation between the filament and formation of nanodiamonds by a heterogeneous nucleation (shown by arrows in Figure 3(b)) on microdiamonds, which were formed after the first pulse. The formation of nanodiamonds (size, 10–20 nm) formed by homogeneous nucleation in between the filaments is shown in Figure 3(c). After the second pulse, it is interesting to note that only Q-carbon and rest of the amorphous carbon melt, while existing microdiamonds do not melt and provide sites for secondary nucleation in the form of nanodots and nanorods (as shown in Figure 3(d)). Here it is clearly shown that diamond melting point is much higher exceeding 5000 K and thus can provide secondary diamond nucleation at a lower temperature around 4000 K. Figure 4(a) shows the formation of microdiamonds, where almost all the Q-carbon is converted into diamond. Figure 4(b) shows a complete conversion of amorphous Q-carbon into a string of microdiamonds. In addition, there are some large areas of Q-carbon in Figure 4(b) that have some diamonds embedded into it but not converted completely into microdiamond. Figure 4(c) shows a triple point of Q-carbon filaments, where the nucleation of diamond is illustrated. The triple points were found to provide easier nucleation sites. After the second pulse, the heterogeneous nucleation of nanodiamonds on existing microdiamonds is clearly shown in Figure 4(d). Stepped and high-index surfaces provide more nucleation site, while the flat surfaces provide less favorable sites. Figure 5(a) shows the formation of nanodiamonds and microdiamonds, which nucleate from the super undercooled region at 0.6 J cm^{-2}. This nucleation and growth can be optimized to cover the entire region with microdiamonds as shown in Figure 5(b). Fig. 5(c) shows the formation of a large-area single-crystal diamond thin film when epitaxial (0001) sapphire or Cu/TiN/Si(100) heterostructures were provided as growth template.[2,3] This also shows the path for integrating diamond

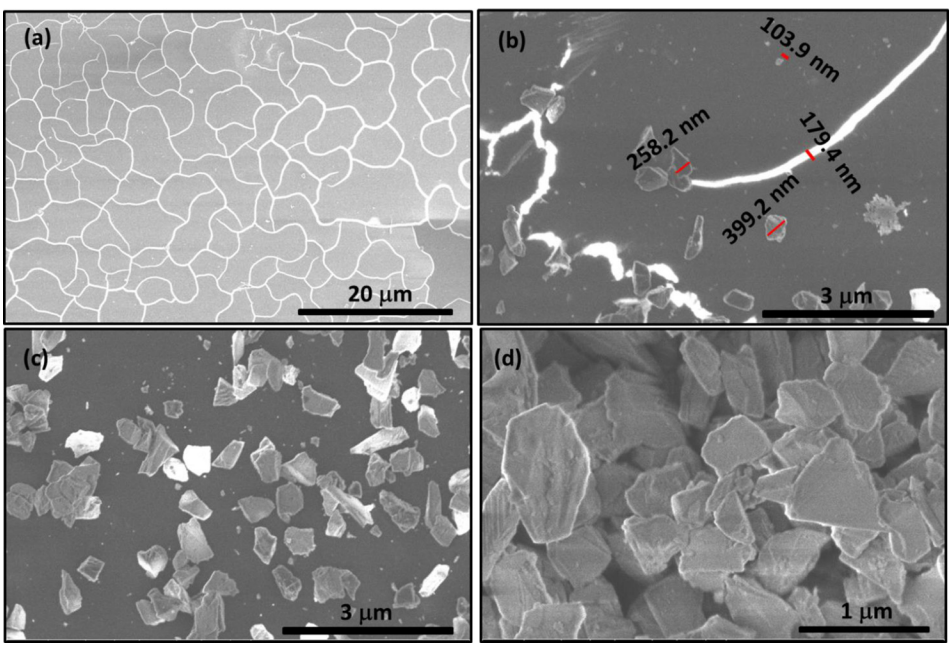

FIG. 2. Formation of Q-carbon and nano- and microdiamonds after one laser pulse: (a) SEM micrograph showing Q-carbon after single laser pulse of ArF laser (wavelength 193 nm, pulse duration 20 ns) at 0.5 J cm^{-2} or outer regions of 0.6 J cm^{-2}; (b) formation of microdiamonds from the filaments toward the edge of 0.6 J cm^{-2} sample; (c) nano- and microdiamonds in the middle of 0.6 J cm^{-2} sample; and (d) only microdiamonds covering the entire area in certain regions of 0.6 J cm^{-2} sample.

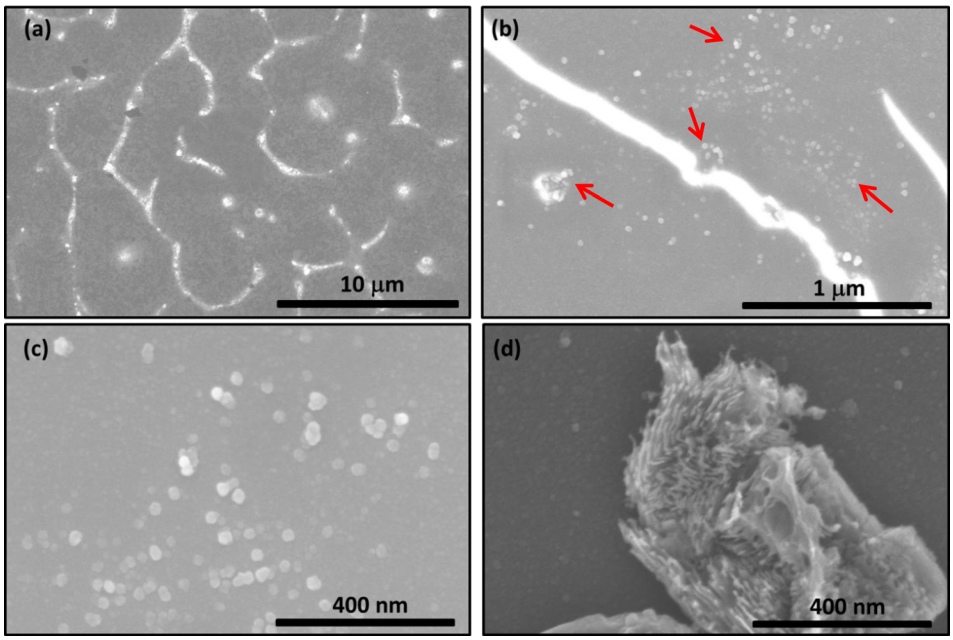

FIG. 3. Formation of microdiamond and nanodiamonds after the second laser pulse: (a) SEM micrograph illustrating the formation of microdiamonds from the Q-carbon filaments; (b) at a higher magnification showing the details of formation of nanodiamonds away from filaments (by homogeneous nucleation) and on the top of existing microdiamonds formation by heterogeneous nucleation; (c) nanodiamonds (10–20 nm) by homogeneous nucleation; and (d) formation of nanorods and nanodots on the existing microdiamond.

thin films on silicon substrates for integrating functionality in next-generation solid state devices.

Raman spectroscopy of Q-carbon and diamond

Figure 6(a) shows Raman results from Q-carbon on sapphire substrate after a single laser pulse of ArF laser (in the outer regions of energy density of 0.6 J cm^{-2}). The Raman spectrum contained a diamond peak at 1333 cm^{-1} with a broad peak around 1350 cm^{-1} and a small peak at 1140 cm^{-1}, associated with strained sp^2 carbon at the interface. A Voigt profile containing convolution of both Gaussian and Lorentzian profiles fits best to the acquired Raman spectrum. The peak positions are fixed at 1140 cm^{-1}, 1333 cm^{-1}, and 1580 cm^{-1}. Evaluation of the ratio of integrals helps us to obtain a 76%–81% sp^3 fraction with the rest being sp^2. The S_1 and S_2 peaks of the spectrum belong to sapphire substrate, the contribution of which was subtracted in sp^3 estimates and is not shown in Figure 6(a) to avoid confusion. A slight up shift of the primary Raman peak is related to quenched-in strains, and a bump at 1140 cm^{-1} in the Q-carbon spectrum is characteristic of sp^2 bonded carbon at the interfaces in nanodiamond. Figure 6(b) shows Raman results from microdiamond on sapphire substrate after a single laser pulse of ArF laser (energy density (0.6 J cm^{-2}). A sharp diamond peak at 1331.54 cm^{-1} along with sapphire peaks S_1 and S_2 (at 1360 and 1375 cm^{-1}) and small G peak of residual unconverted amorphous graphite are observed. The Raman shift ($\Delta\omega$) is related to $\Delta\omega$ (in cm^{-1}) $= 2.2 \pm 0.10\ cm^{-1}\ GPa^{-1}$ along the [111] direction, $\Delta\omega$ (in cm^{-1}) $= 0.73 \pm 0.20\ cm^{-1}\ GPa^{-1}$ along the [100] direction, and $\Delta\omega$ (in cm^{-1}) $= 3.2 \pm 0.23\ cm^{-1}\ GPa^{-1}$ for the hydrostatic

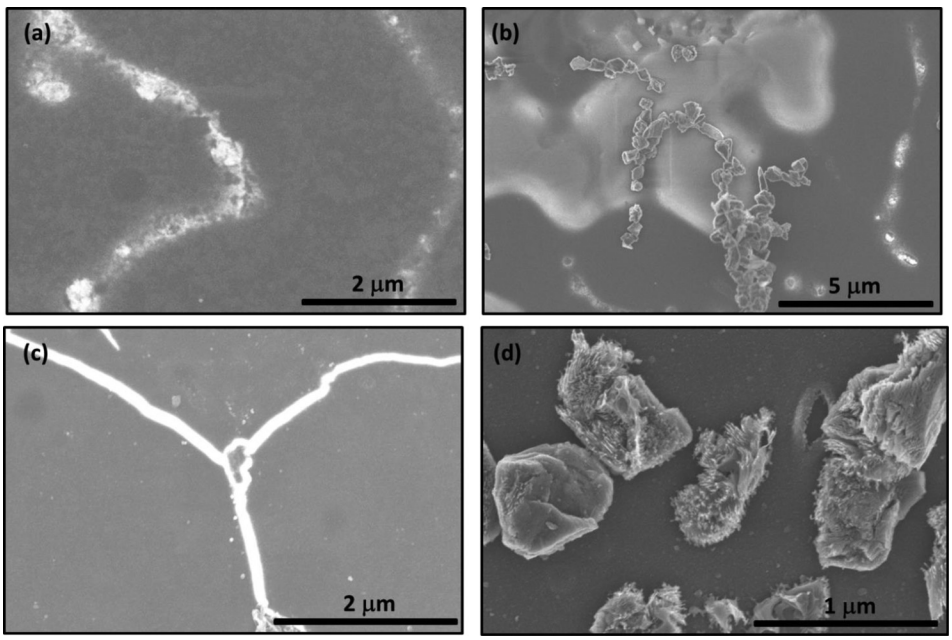

FIG. 4. SEM of heterogeneous nucleation of nano- and microdiamonds; (a) shows the formation of microdiamonds, where almost all the Q-carbon is converted into diamond; (b) shows a complete conversion of amorphous Q-carbon into a string of microdiamonds. There are also some large areas of Q-carbon in (b) that have some diamonds embedded into it but not converted completely into diamond; (c) shows a triple point of Q-carbon filaments, where the nucleation of diamond is illustrated; (d) the heterogeneous nucleation of nanodiamonds on existing microdiamonds after second laser pulse.

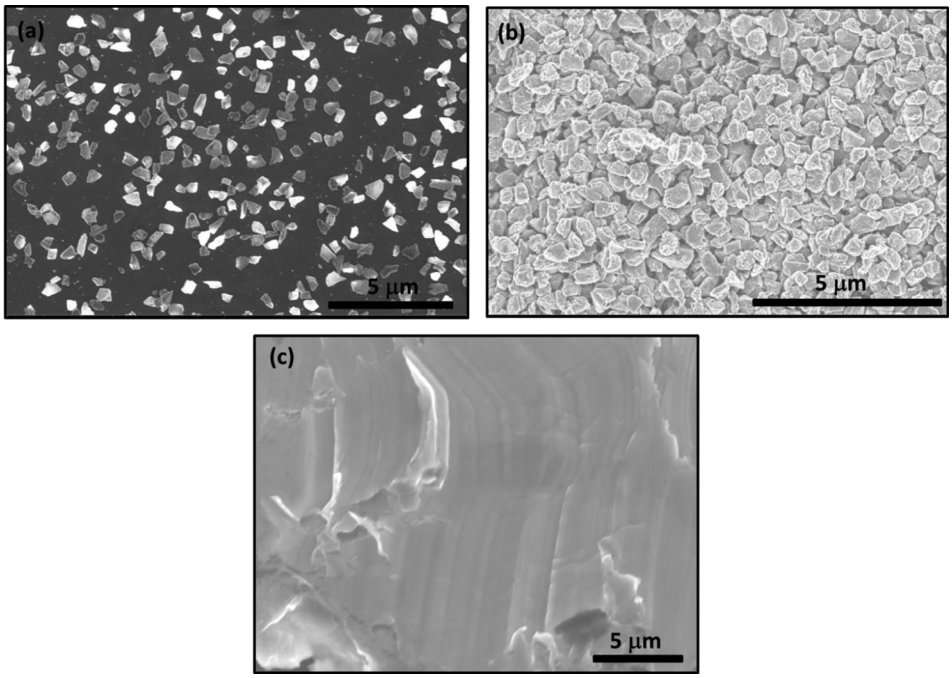

FIG. 5. Formation of nanodiamonds and microdiamonds after two pulses of 0.6 J cm^{-2} pulse: (a) a mixture nano and microdiamonds of different morphology; (b) microdiamonds covering entire area (with some nanodiamonds on the top); and (c) large-area single-crystal diamond thin film on Cu/TiN/Si(100) epitaxial template.

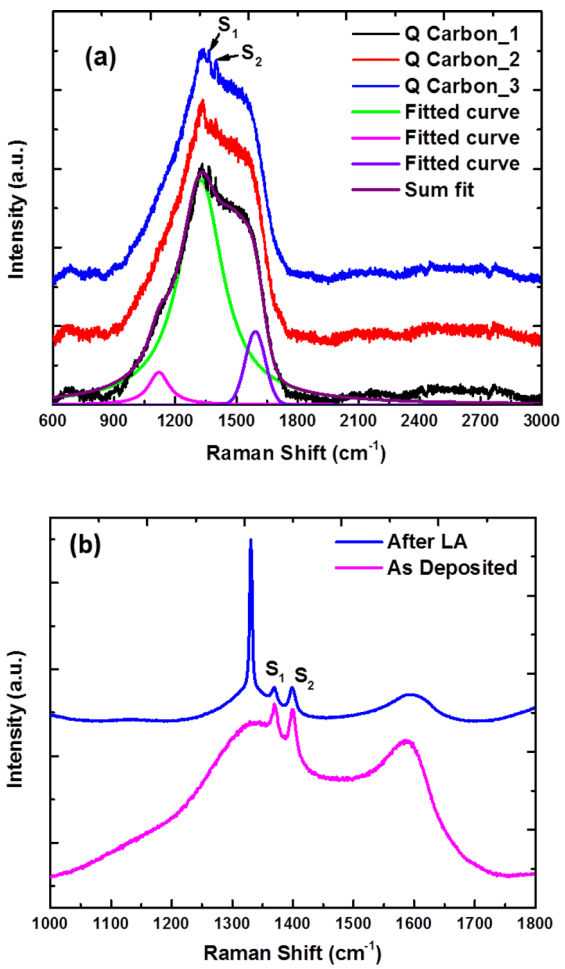

FIG. 6. Raman characterization using laser wavelength (633 nm) of Q-carbon and diamond: (a) Raman spectra from three different regions of Q-carbon with embedded diamond, showing diamond peak at 1331 cm^{-1} and diamond-like carbon peaks at 1140 cm^{-1} and 1580 cm^{-1}. The sp^3 fraction derived is in the range of 75%–85%, the S_1 and S_2 peaks belong to sapphire; (b) Raman spectra from microdiamond region and as-deposited DLC film with sp^3 fraction (52%).

component.[19] The biaxial stress in thin films can be described as a combination of two-thirds hydrostatic and one-third uniaxial stress. The biaxial stress can be estimated using $\sigma = 2\,\mu\,(1+\upsilon)/(1-\upsilon).\Delta\alpha.\Delta T$, where μ is shear modulus, υ is Poisson's ratio, $\Delta\alpha$ is the change in thermal coefficient of expansion, and ΔT is the change in temperature.

HRTEM and EELS from Q-carbon and diamond

The HRTEM and EELS characterization of Q-carbon and diamond were carried out using the cross-section sample containing nano- and microdiamonds on sapphire as shown in a SEM image of Fig. 7. Figure 8(a) is a cross-section HRTEM image from a diamond microcrystallite, where the ⟨110⟩ cross-section has two sets of {111} planes and ⟨110⟩ columns of diamond are clearly imaged. The characteristic ⟨110⟩ diamond selected-area-diffraction pattern is included in the inset. The HRTEM also shows the presence of a twin

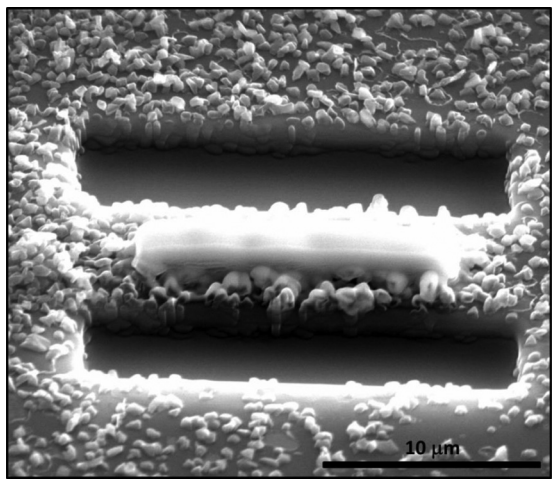

FIG. 7. SEM image of cross-section TEM sample containing nano- and microdiamonds on sapphire.

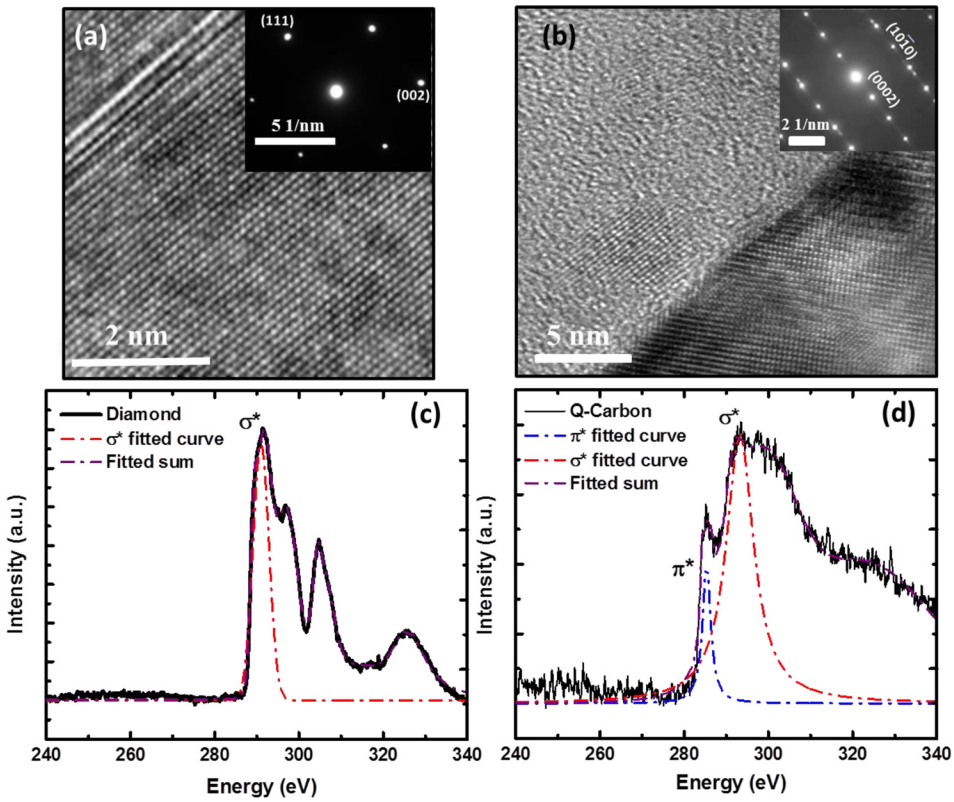

FIG. 8. High resolution TEM and EELS from diamond and Q-carbon from a cross-section TEM sample with diamond on sapphire using FEI Titan: (a) ⟨110⟩ HRTEM image showing individual columns of atoms with resolution of 0.18 nm with inset ⟨110⟩ electron diffraction pattern from (111) epitaxial diamond on (0001) sapphire; (b) HRTEM from Q-carbon showing amorphous structures and some nanodiamonds with inset ⟨−2110⟩ selected-area-diffraction pattern of sapphire; (c) EELS spectrum from microdiamond (energy resolution, 0.15 eV) showing a sharp edge at 288 eV with a peak at 292 eV; and (d) EELS spectrum from Q-carbon has a sloping edge at 285 eV with a broad peak at 292 eV.

in a diamond thin film that has grown epitaxially on sapphire by planar matching epitaxy with ⟨111⟩dia//⟨0001⟩sap and ⟨110⟩dia//⟨−2110⟩sap. Figure 8(b) shows HRTEM image (with inset ⟨−2110⟩ selected-area diffraction pattern from sapphire) from the Q-carbon near the sapphire substrate, where it has mostly amorphous structure with a few nanodiamonds embedded into it. To investigate the details of bonding characteristics, EELS studies were carried out using aberration corrected STEM-FEI Titan 80–300 with an energy resolution of 0.15 eV. Figure 8(c) is an EELS spectrum from diamond, showing characteristic sp^3 (σ^*) bonding. The spectrum contains a sharp edge at 288 eV with a peak at 292 eV, corresponding to sp^3 (σ^*) bonding, which is a signature EELS spectrum for diamond. The characteristic EELS spectrum from the Q-carbon is shown in Figure 8(d), which has a sloping edge at 285 eV with a broad peak at 292 eV. From the Voigt profile fit of the EELS spectrum, the sp^3 was estimated to be about 80% and 20% sp^2; this is consistent with Raman results from the Q-carbon and is also shown in Figure 8(d). The peak position for σ^* and π^* edges are fixed at 292 eV and 285 eV, respectively. All the other fitted peaks are not shown to avoid confusion.

Formation of diamond nano and microneedles

When carbon melts around 4000 K in a highly undercooled state near the carbon film/sapphire interface, there is a reduction in volume or shrinkage. Because the carbon in the molten state is metallic, carbon atoms assume a closed packed structure, which can be quenched into the Q-carbon. This shrinkage and internal melting result in the formation of bubbles that burst out, and single-crystal diamond micro- and nanoneedles grow out of these areas, depending on the size of the bubble. The formation of 2–3 μm long microneedles will require growth velocities of the order of 5–10 ms^{-1} with estimated 250–500 ns melt lifetime, which is only possible under crystal growth from melt under highly undercooled state of carbon.

The diamond structure determination and phase identification have been also carried out using EBSD, also known as backscatter Kikuchi diffraction (BKD), by using field-emission scanning electron microscope. This is a powerful

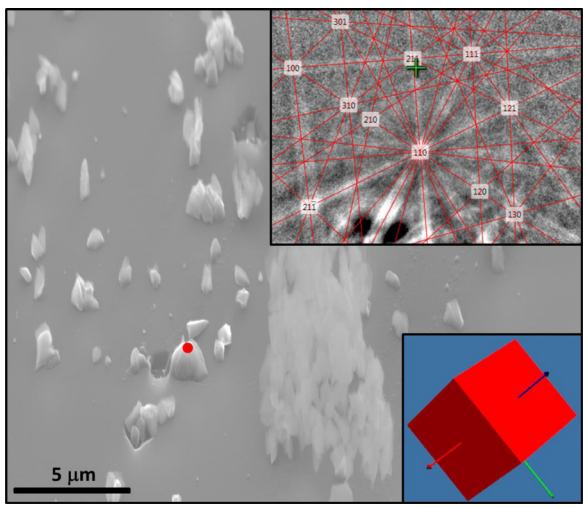

FIG. 9. Electron Backscatter Diffraction (EBSD) patterns, also known as backscatter Kikuchi diffraction (BKD) patterns, from microdiamonds growing out the Q-carbon near the sapphire interface: ⟨110⟩ EBSD Kikuchi pattern from the encircled nanodiamond (red); and relative orientation of the diamond microcrystallite.

technique to determine the crystal structure of nano- and microdiamonds (with resolution of 10 nm) and their relative orientations with respect to the substrate. In EBSD, a stationary electron beam strikes a tilted crystalline sample, and the diffracted electrons form a pattern on a fluorescent screen. This pattern is characteristic of the crystal structure and orientation of the sample region from which it was generated. It provides the absolute crystal orientation with sub-micron resolution. The results are shown in Figure 9 from a microdiamond with SEM micrograph, characteristic diamond Kikuchi pattern, and orientation relationship of the diamond with respect to the substrate normal. The microdiamonds grow here in the form of microneedles up to 2 μm in length. These microneedles grow out of the Q-carbon formed near the sapphire interface through the carbon over layers that must be molten during the growth of these needles. The formation of such long microneedles can occur only in the liquid phase where diffusivity is of the order of 10^{-4} cm^2 s^{-1}. The residual amorphous carbon can be etched away by hydrogen and oxygen plasma, leading pristine diamond structure. Fig. 10(a) shows SEM of microneedles, and corresponding Raman results are shown in Fig. 10(b) where only a very sharp Raman diamond peak at 1136 cm^{-1} along with a sharp substrate peak are observed. The inset shows EBSD with the characteristic diamond Kikuchi pattern. We propose that the formation of microneedles occurs by rapid explosive recrystallization where nanodiamonds nucleate from the Q-carbon and grow rapidly by liquid mediated explosive recrystallization[20] to lengths of the order of microns. The length of a nanoneedle or microneedle can be determined by growth velocity in the liquid phase, which is given by $v = K_s T_m/((D\tau)^{0.5}\rho L)$, K_s is thermal conductivity of sapphire (5.65 W m^{-1} K^{-1}), T_m is melting point of carbon (4000 K), D is the thermal diffusivity (1.0×10^{-6} m^2 s^{-1}), ρ is mass density of liquid carbon (3.5 g cm^{-3}), and L is latent heat of carbon (8000 J g^{-1})[6]. Substituting these values, a rough estimate of the growth velocity is obtained to be 2–3 ms^{-1}, giving the length of microneedle 1–2 μm.

Diamond deposition on heat sensitive polymer substrates

By using ArF pulsed excimer laser, heating can be controlled spatially and temporally in such a way that while amorphous carbon films are melted, substrates stay close to ambient temperatures. Thus diamond thin films can be formed on heat-sensitive plastics and polymer substrates. Fig. 11(a) shows SEM micrograph of microdiamonds and nanodiamonds with average grain size of 500 nm and 30 nm, respectively, on a HDPE substrate. Because these diamond grains are formed during rapid quenching, the grains contain

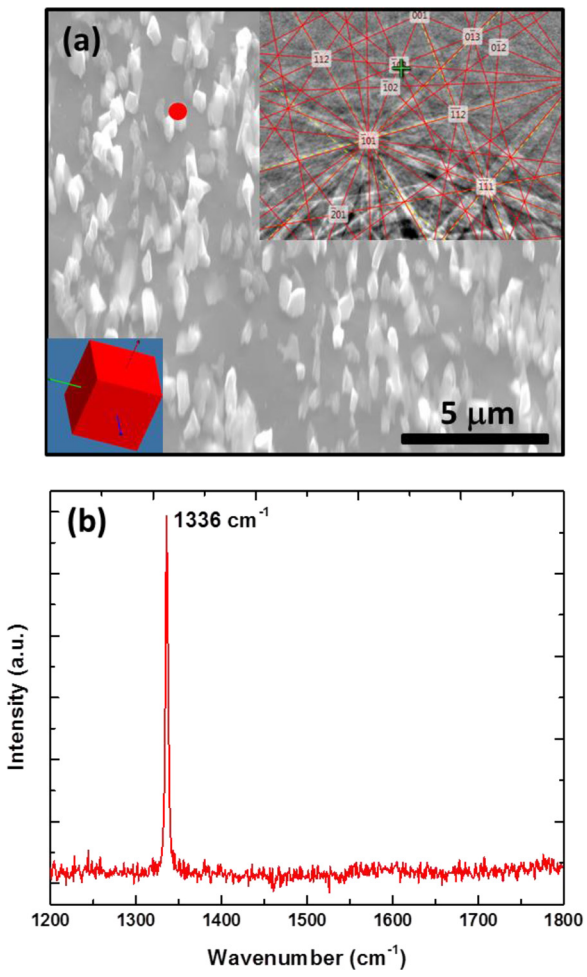

FIG. 10. Formation of diamond microneedles: (a) SEM micrograph and (b) Raman spectrum with a peak at 1336 cm^{-1}. The inset in (a) shows electron backscatter diffraction pattern of diamond.

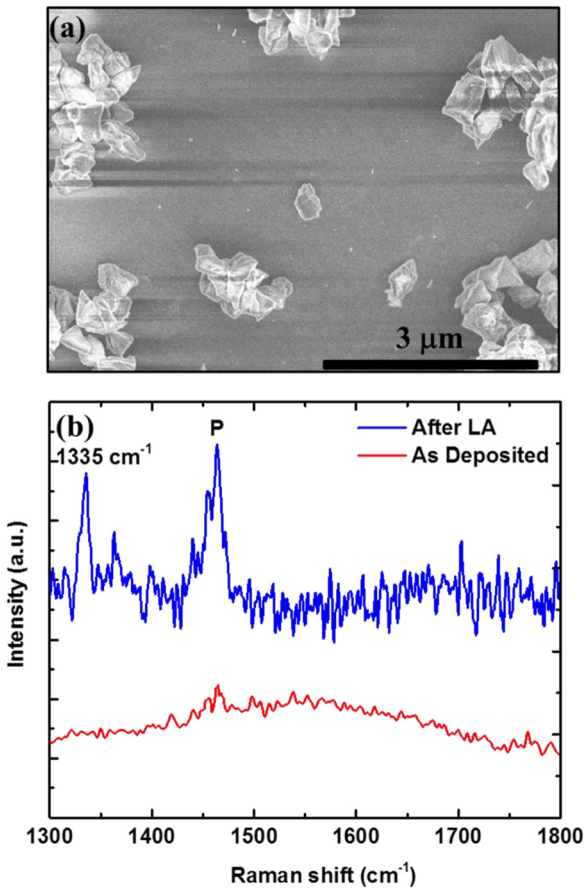

FIG. 11. Formation of diamond on HDPE: (a) SEM micrograph and (b) characteristic Raman spectrum before and after laser annealing with 0.8 J cm^{-2}, containing diamond peak at 1335 cm^{-1} and HDPE peak at 1464 cm^{-1}.

high-index facets unlike low index facets produced during CVD processes. The high-index facets have been shown to be catalytically more and provide nucleation sites for subsequent diamond growth. The Raman spectrum, shown in Fig. 11(b), contains characteristic diamond peak at 1335 cm^{-1} and HDPE peak at 1464 cm^{-1} after the laser treatment. The Raman spectrum from as-deposited amorphous diamondlike carbon films contains a broad peak around 1350 cm^{-1} from which sp^3 was extracted to be 45%.

Ferromagnetism in Q-carbon

The Q-carbon samples with sapphire substrates were investigated for ferromagnetic properties by using the PPMS. The results showed RTFM in Q-carbon as shown in Figure 12, where the M vs. H curve has finite coercivity (~150 Oe) at room temperature. It is interesting to note that saturation magnetization in the M-H plots decreases only slightly with temperature, and coercivity increases only slightly from ~150 Oe at 300 K to ~200 Oe at 10 K. The saturation magnetization $M_s(T)$ is given by $M_s(T) = M_s(0)$ tanh $[(M_s(T)/M_s(0))/(T/T_c)]$, where $M_s(0)$ is saturation magnetization at 0 K and T_c is Curie temperature. Using this equation, a decrease by 10% in $M_s(T)$ at 300 K gives a rough estimate for the Curie temperature of Q-carbon about 500 K. From the saturation magnetization value of 20 emu g^{-1}, the magnetic moment in the Q-phase is estimated to be 0.4 μ_B (Bohr magneton) per atom. Controlled samples with only diamond, diamond-like carbon, and sapphire substrate showed only diamagnetism, which was subtracted in the plot as shown in Figure 12. The magnetic force microscopy measurements (in the inset) from a triple point show a granular (about 50 nm diameter) magnetic contrast in the Q-carbon and a dark contrast from diamagnetic diamond. The granular features reflect the distribution of sp^3 and sp^2 bonded carbon, where the amorphous grains have mostly sp^3 with sp^2 bonded carbon at the boundaries. The diamond nucleates preferentially at the triple points of Q-carbon. The magnetic contrast from MFM was compared carefully with EFM contrast to distinguish it from electrostatic field contrast from the surface. The origin of magnetism may be related to unpaired spins generated by mixing of sp^3 and sp^2 bonding in the Q-carbon. This is the first direct evidence for bulk intrinsic ferromagnetism in carbon without the presence of hydrogen or any other impurities. Ferromagnetism in carbon has been observed near the surface in proton and carbon ion irradiated HOPG, where its origin was linked to π-electrons and hydrogen-defect complexes.[21] Ferromagnetism has been predicted theoretically[22] in bulk carbon containing 50% sp^2 and 50% sp^3 hybridized carbon. The structure of this ferromagnetic phase is predicted to be rhombic type ($a = 0.2608$ nm, $b = 0.3961$ nm, $c = 0.5289$ nm with $\alpha = \beta = \gamma = 90°$), which is intermediate between the graphite and diamond structure with mass density of 2.9 g cm^{-3}. However, in our experiments, amorphous carbon with 50% sp^2 and 50% sp^3 is found to be diamagnetic. This amorphous carbon turns magnetic only when it is melted under super undercooled state and quenched to form Q-carbon. Experimentally, ferromagnetism has been also observed[23] in polymerized state of rhombohedral C_{60}, where ferromagnetic order results from unpaired spins with magnetic moment estimated as 0.4 μ_B per atom in agreement with our value. It should be pointed out that no ferromagnetism was observed in pristine fullerene or depolymerized C_{60} samples. It has been observed that under high pressures (~17 GPa) and ambient temperatures,[24] about 50% of π bonds in graphite convert into σ bonds. It would be interesting to see if the unpaired electrons associated with π bonds lead to ferromagnetic order under high pressures where mass density is higher.

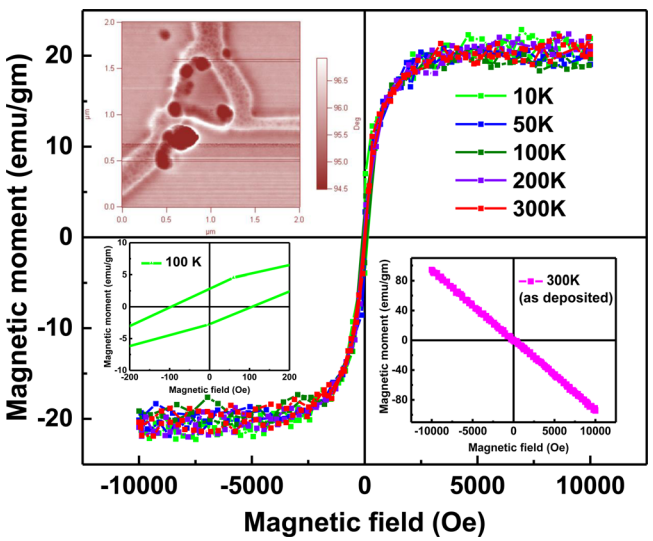

FIG. 12. Bulk ferromagnetism in carbon: M-H curves at different temperatures from sample containing Q-carbon filaments with a higher magnification inset at 100 K. The insets also show diamagnetic behavior before the laser treatment and MFM measurements from a triple point with a granular (about 50 nm diameter amorphous sp^3 carbon) magnetic contrast in the Q-carbon and a dark contrast from diamagnetic crystalline diamond.

Enhanced field emission, electrical conductivity, and hardness of Q-carbon

Surface potential measurements were carried out to assess the field emission characteristics of the Q-carbon phase. The surface potential measurements were carried out using KPFM on the Q-carbon filaments, which were embedded into diamond-like carbon. The results shown in Fig. 13 show a lower surface potential compared to diamond-like carbon up to 40 meV, indicating higher field emission potential compared to diamond-like carbon, which already has higher field emission properties. It is interesting to note that surface potential decrease at nanodiamonds, which are embedded into the Q-carbon filaments, is lower than Q-carbon values. These results on KPFM surface potential measurements are consistent with secondary electron emission contrast in the SEM images, showing significantly enhanced contrast for the Q-carbon filaments. The shrinkage at the Q-carbon filaments was found to be about 35–40 nm, indicating that the mass density of Q-carbon is considerably higher and C-C bond length shorter than that of as-deposited amorphous carbon.

The resistivity of diamond-like carbon films was measured before and after the laser treatment, where there are embedded filaments. Preliminary results showed a significant

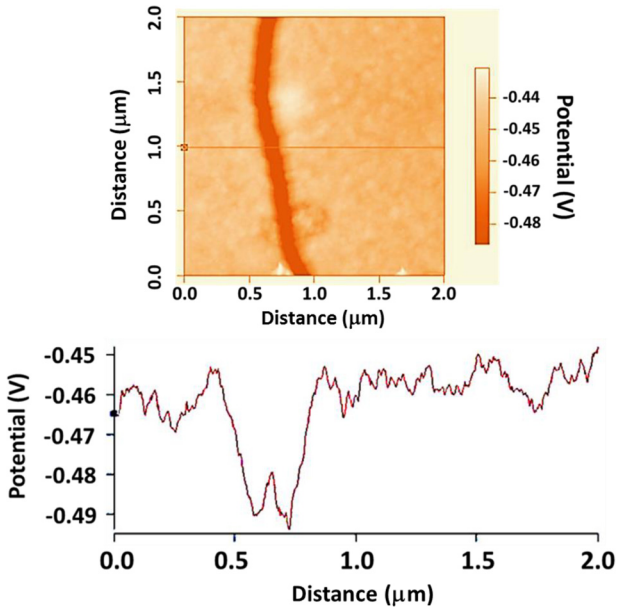

FIG. 13. KPFM measurements showing negative surface potential associated with Q-carbon compared to the matrix of diamond and diamond-like carbon, which already have low surface potential.

decrease in resistivity after the laser treatments in samples with embedded filaments. The decrease in resistivity with increasing temperature showed characteristics semiconducting behavior up to 125 K and a semiconductor-to metal transition as shown Fig. 14. Depending upon the quenching rate, we can control the semiconductor state and preserve it at room temperature. The Q-carbon is formed as a result quenching from the melt, which is expected to be metallic. During melting, there is over 10% decrease in volume, and upon quenching, the structure is amorphous with a high sp^3 to sp^2 fraction. Thus Q-carbon in this state is amorphous and exhibits semiconducting behavior. Two resistivity transitions observed at 125 K (semiconductor to metal) and 185 K (metal to semiconductor) may be part of Q-carbon characteristics. Further studies are underway to unravel the contributions of competing scattering mechanisms (variable range hopping, electron-electron and electron-phonon scattering) as a function of temperature.

The formation Q-carbon occurs as a result of quenching of the super undercooled state of liquid carbon. The liquid carbon has metallic bonding,[1] which promotes the close packing of carbon atoms with atomic radius of 0.070 nm. Upon quenching, these carbon atoms arrange themselves mostly into fourfold coordination (sp^3 bonded carbon, covalent radius 0.077 nm) with the remainder arranging themselves into threefold coordination (sp^2 bonded carbon). The relative fraction for sp^3 bonded carbon varies from 70% to 85%. Assuming a homogeneous mixture, the effective radius is calculated to be 0.075 nm. Because bulk modulus (B in GPa) varies, $N_c/4\ (1972-220I)d^{-3.5}$, where N_c is the coordination number, I is the iconicity parameter accounting for the charge transfer, and d is covalent radius in (A).[25,26] Considering the predominance of first nearest neighbors in the amorphous structure of Q-carbon, a rough estimate can lead to lead to a few percentage higher hardness than diamond. The hardness of Q-carbon filaments was measured by using nanoindenter measurements. These filaments of Q-carbon were embedded in the diamond-like carbon. The relative hardness of the Q-carbon filaments was measured to be in the range of 35 GPa compared to 21 GPa for the diamond-like carbon. Thus Q-carbon is harder by over 60% compared to diamond-like carbon, suggesting that hardness of Q-carbon may exceed that of diamond as a result of shorter average C-C bond length of Q-carbon. The Q-carbon phase was also found to be quite stable as a function of temperature. The Raman spectra (Fig. 15) as function of second laser pulse at 0.2, 0.4, 0.5, and 0.6 J cm^{-2} showed almost no change up to 0.4 J cm^{-2}, indicating that Q-carbon is quite stable against thermal heating. Only after 0.5 and 0.6 J cm^{-2}, when temperatures exceed 4000 K, there are observable changes in the Raman spectra. The estimated temperature using Singh and Narayan model (SLIM) calculations after 0.2, 0.4, and 0.5 J cm^{-2}, are 1330 K, 2665 K, and 3330 K, respectively.[6]

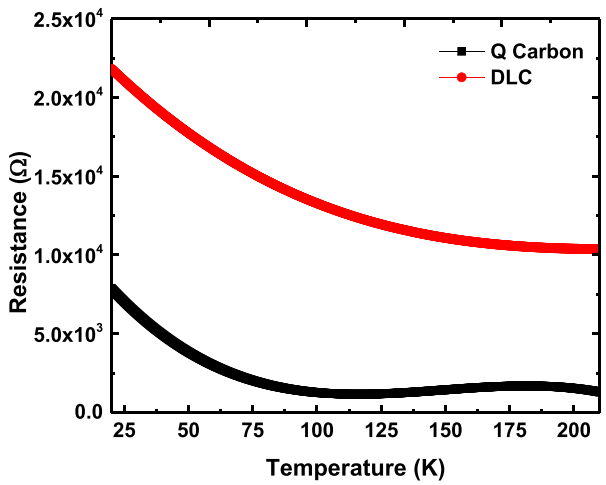

FIG. 14. Resistance versus temperature before (DLC) and after in the presence of Q-carbon.

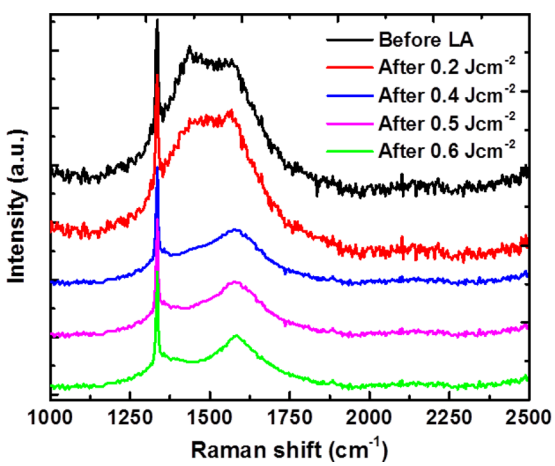

FIG. 15. Raman spectra of Q-carbon and after laser irradiation with energy densities of 0.2, 0.4, 0.5, and 0.6 J cm^{-2}.

DISCUSSION

The formation of nanodiamond in the absence of a template occurs as a result of homogeneous nucleation of diamond phase from the highly undercooled pure carbon. Fig. 16 shows a homogeneous nucleation of diamond 2–8 nm diameter after ArF laser irradiation. At a higher magnification, we find that these nanodiamonds down to 2 nm size are crystalline. For a homogenous nucleation of diamond from highly undercooled state of pure carbon, the Gibbs free energy of diamond nuclei (ΔG_T) consists of gain in volume energy (ΔG_V) and expense of surface free energy (ΔG_S) terms and can be written as

$$\Delta G_T = \Delta G_V + \Delta G_S, \tag{1}$$

$$\Delta G_T = \frac{-4}{3}\pi r^3 \frac{\rho}{M_m}\frac{\Delta H_m}{T_m}\Delta T_u + 4\pi r^2 r_s, \tag{2}$$

where "r" is the radius of diamond nucleus, $(\frac{\rho}{M_m}\frac{\Delta H_m}{T_m}\Delta T_u)$ is the gain in free energy for the formation of diamond nucleus from the undercooled state, ΔT_u is the undercooling from T_m to T_r (temperature of nucleation), ρ is the solid diamond density, M_m is the molar mass, ΔH_m is the latent heat of melting, T_m is the melting point of carbon, and r_s is the average surface free energy between diamond nuclei and undercooling carbon liquid.

The maximum of ΔG_T^* corresponds to the diamond reaction barrier at a critical size of r*, where

$$r^* = \frac{2r_s T_m M_m}{\Delta H_m \Delta T_u \rho}, \tag{3}$$

$$\Delta G_T^* = \frac{16\pi r_s 3T_m^2 M_m^2}{3\Delta H_m^2 \Delta T_u^2 \rho^2}. \tag{4}$$

Rate of nucleation (I) is govern by

$$I = A\exp\frac{-\Delta G_T^*}{KT_r}, \tag{5}$$

where $T_r = T_m - \Delta T_u$, $A = n(kT/h)\exp(-\Delta F_A/kT)$, I = number of diamond nuclei $cm^{-3}\ s^{-1}$, n = number density of atoms, and ΔF_A is free energy of activation across the liquid-solid interface. Our calculated values for 5 and 10 nm diamond observed crystallite size lead to A values of 10^{25} and $10^{24}\,cm^{-3}\,s^{-1}$, respectively, which are consistent with our earlier results on homogeneous nucleation in super undercooled amorphous silicon.[10,11] This is consistent with A values for diamond nucleation from first principles calculations.[27] At the formation temperature, T_r, the free energy of metastable diamond, highly undercooled carbon liquid, and amorphous diamond like carbon become equal.

Diamond nucleation is difficult due to large r_s but the large undercooling ΔT_u drives the r* lower and helps the nucleation. Also ΔG^* is lowered considerably under large undercooling due to ΔT_u^{-2} dependence. The lower ΔG^* also enhances nucleation rate of nanodiamond from the highly undercooled state, and these nanodiamonds provide a seed for microdiamond growth. It should be emphasized that the undercooling should be retained for a sufficient time for diamond nanocrystallite not only able to nucleate but to grow to desired sizes. For a 10 nm size nanodiamond, the estimated growth time is about 5–10 ns. This time requirement emphasizes the importance of low thermal conductivity of the substrate during rapid pulse laser heating. A rough estimate of r^* for diamond nuclei from Equation (3) is 5–10 A, where diamond surface free energy r_s is 0.6 J m^{-2}, $T_m = 4000$ K, $\Delta H_m = 1.0$ eV/atom, $\Delta T_u = 500$–1000 K, and $\rho = 3.5$ g m/cm^{-3}. Thus diamond nucleation from highly super undercooled carbon can occur readily.

Basharin *et al.*[28,29] have estimated the temperature dependence of Gibbs free energy of graphite, metastable liquid carbon and diamond at a low pressure of 0.012 GPa of helium and found that free energy of liquid carbon can be equal to that of diamond at 4160 ± 50 K; this is considerably lower than melting point of liquid graphite at a pressure of 0.012 GPa of helium. Fig. 17 shows variation of Gibbs free energy as a function of temperature for graphitic carbon (G_g), liquid carbon (G_{liq}), and diamond (G_d) near our ambient temperature of processing. According to this free energy diagram, amorphous Q-carbon is formed at the highest undercooling T_q, and diamond is nucleated at slightly higher temperature of T_d. It should be mentioned that Basharin *et al.*[28] tried to quench diamond using 1 ms pulsed laser melting (wavelength of $\lambda = 1.06\,\mu$m and a power of 10 kW) of HOPG graphite

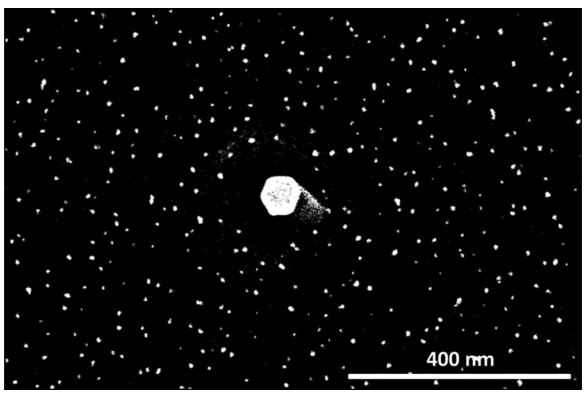

FIG. 16. Homogeneous nucleation of diamond (2–8 nm diameter) after laser irradiation at energy density of 0.55 J cm^{-2}.

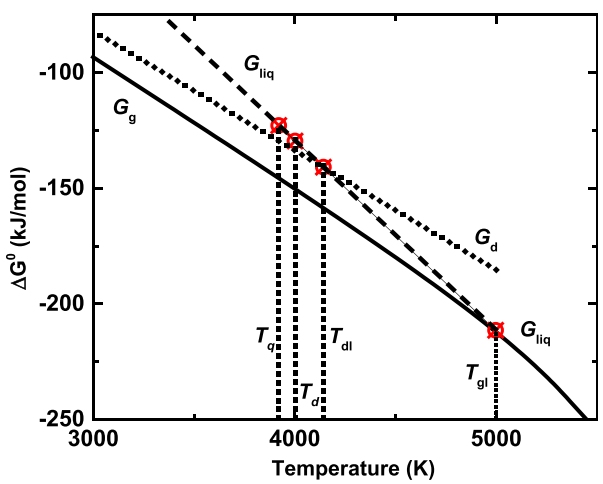

FIG. 17. Gibbs free energy as a function of temperature for graphitic carbon (G_g), liquid carbon (G_{liq}), and diamond (G_d) following.[28] The amorphous Q-carbon is formed as result of quenching from T_q and diamonds nucleate at T_d.

with limited success due to significantly lower undercooling with 1 ms lasers on a crystalline graphite substrate. Our experiments on HOPG graphite even with nanosecond lasers failed to nucleate diamond due to a lower undercooling.

Undercooling during nanosecond laser (KrF laser $\lambda = 0.248\ \mu$m) melting has been measured in crystalline Ge and Si using nanosecond resolution time-resolved x-ray diffraction in a synchrotron.[30,31] These results showed undercooling as high as 110 ± 30 K on (111) Si during $\sim 10\ \text{ms}^{-1}$ melting and $\sim 6\ \text{ms}^{-1}$ regrowth velocity. Thus the undercooling is crystalline Ge and Si is roughly half that predicted theoretically for amorphous Ge and Si. The undercooling was also found to be orientation and regrowth velocity dependent: ~ 5 K/m s on (100) Ge and ~ 20 K/m s on (111) Ge.

Bonding and structure of liquid carbon have been studied using time-resolved x-ray absorption spectroscopy,[32] and results compared with first-principles molecular dynamics simulations.[33] These results suggest that local bonding structure of the liquid can be varied from a mixture of two- and threefold coordinated atoms at low density (1.27 g cm^{-3}) to fourfold coordinated atoms at high density (3.02 g cm^{-3}). The latter liquid structure correspond to liquid carbon structure at high pressures. Thus the structure of diamond-like carbon (containing $>20\%$–40% sp^3 bonding) at low pressures under super undercooling is similar to the structure of liquid carbon at high pressures, where conversion into diamond phase occurs.

In summary, we have created a novel phase of carbon by nanosecond laser melting and quenching carbon from the super undercooled state in the form of thin films or filaments. This Q-carbon has amorphous structure with some embedded nanocrystalline diamonds the number density of which is determined by the nucleation time available for growth. The Raman spectrum from the Q-carbon shows a very large fraction of sp^3 (75%–85%) bonded carbon, along with diamond peak at 1333 cm^{-1} and sp^2 bonded peaks at 1140 cm^{-1} and 1580 cm^{-1}. Nanodiamonds, microdiamonds, nanoneedles, microneedles, and thin films are readily formed from the Q-carbon depending upon the time allowed for growth during the quenching period. The large-area single-crystal thin films of diamond are grown by providing epitaxial templates, such as (0001) sapphire where growth occurs by planar domain matching epitaxy[34] with $\langle 111\rangle$dia//$\langle 0001\rangle$sap and in plane $\langle 110\rangle$dia//$\langle -2110\rangle$sap. The diamond can be doped with B (p-type) and N (n-type) as result of crystal growth from undercooled melt. The Q-carbon is found to be ferromagnetic at room temperature and above the origin of which is linked to the π-electrons. This ferromagnetism can explain now magnetism in the Earth's mantle and other planets with liquid and quenched in carbon. It also solves the mystery of formation of natural diamonds in the planets. Recently, similar results have been obtained for the BN (boron nitride) system, where Q-BN is formed upon quenching the super undercooled liquid and hBN is converted into cBN.[35] This method allows synthesis and processing of nanodots, microcrystals, nanoneedles, microneedles, and single-crystal thin films of diamond and cBN rather inexpensively on practical and heat-sensitive substrates for a variety of applications ranging from abrasive powders, novel catalytic properties, smart displays, and myriads of biomedical and microelectronic and nanoelectronic applications with a maximum impact on humankind.

ACKNOWLEDGMENTS

We are grateful to Fan Family Foundation Distinguished Chair Endowment for Professor J. Narayan, and this research was partly funded by the National Science Foundation. We are also very pleased to acknowledge technical help and useful discussions with John Prater, Jim LeBeau, Weizong Xu, Xiahan Sang, Roger Narayan, Jerry Cuomo, and Benjamin Hoffman.

[1]F. P. Bundy, W. A. Bassett, M. S. Weathers, R. J. Hemley, H. U. Mao, and A. F. Goncharov, Carbon **34**, 141 (1996).
[2]J. Narayan, V. P. Godbole, and C. W. White, Science **252**, 416 (1991).
[3]J. Narayan and A. Bhaumik, APL Mater. **3**, 100702 (2015); US patent pending 62/245,018 (2015); US patent pending 62/202,202 (2015).
[4]J. C. Angus and C. C. Hayman, Science **241**, 913 (1988).
[5]Y. Gogotsi, S. Welz, D. A. Ersoy, and M. J. McNallan, Nature **411**, 283 (2001).
[6]R. K. Singh and J. Narayan, Mater. Sci. Eng., B **3**, 217 (1989).
[7]E. P. Donovan, F. Spaepen, D. Turnbull, J. M. Poate, and D. C. Jacobson, Appl. Phys. Lett. **42**, 698 (1983).
[8]J. Narayan and C. W. White, Appl. Phys. Lett. **44**, 35 (1984).
[9]J. Narayan, C. W. White, O. W. Holland, and M. J. Aziz, J. Appl. Phys. **56**, 1821 (1984).
[10]R. F. Wood, D. H. Lowndes, and J. Narayan, Appl. Phys. Lett. **44**, 770 (1984).
[11]D. H. Lowndes, R. F. Wood, and J. Narayan, Phys. Rev. Lett. **52**, 561 (1984).
[12]J. W. Cahn, S. R. Coriell, and W. J. Boettinger, in *Laser and Electron Beam Processing of Materials*, edited by C. W. White and P. S. Peercy (Academic Press, 1980), p. 89.
[13]J. Narayan, G. L. Olson, and O. W. Holland, MRS Proc. **4**, 183 (1981).
[14]B. G. Bagley and H. S. Chen, AIP Conf. Proc. **50**, 97–101 (1979).
[15]C. W. White, D. M. Zehner, J. Narayan, O. W. Holland, B. R. Appleton, and S. R. Wilson, MRS Proc. **13**, 287 (1982).
[16]C. W. White, J. Narayan, and R. T. Young, Science **204**, 461 (1979).
[17]C. W. White, P. P. Pronko, S. R. Wilson, B. R. Appleton, J. Narayan, and R. T. Young, J. Appl. Phys. **50**, 3261 (1979).
[18]J. Narayan, J. Appl. Phys. **52**, 1289 (1981).
[19]S. Prawer and R. J. Nemanich, Philos. Trans. R. Soc., A **362**, 2537 (2004).
[20]J. Narayan, Mater. Lett. **2**, 219 (1984).
[21]H. Ohldag, T. Tyliszczak, R. Höhne, D. Spemann, P. Esquinazi, M. Ungureanu, and T. Butz, Phys. Rev. Lett. **98**, 187204 (2007).
[22]A. A. Ovchinnikov and I. L. Shamovsky, J. Mol. Struct.: THEOCHEM **251**, 133 (1991).
[23]T. L. Makarova, B. Sundqvist, R. Hohne, P. Esquinazi, Y. Kopelevich, P. Schraff, V. Davydov, L. S. Kashevaova, and A. V. Rakhmanina, Nature **413**, 716 (2001).
[24]W. L. Mao, H.-K. Mao, P. Eng, T. Trainor, M. Newville, K.-C. Kao, D. Heinz, J. Shu, Y. Meng, and R. J. Hemley, Science **302**, 425 (2003).
[25]A. K. Sharma and J. Narayan, Int. Mater. Rev. **42**, 137 (1997).
[26]A. Y. Liu and M. L. Cohen, Science **245**, 841 (1989).
[27]L. M. Ghiringhelli, C. Valeriani, J. H. Los, E. J. Meijer, A. Fasolino, and D. Frenkel, Mol. Phys. **106**, 2011 (2008).
[28]A. Y. Basharin, V. S. Dozhdikov, A. V. Kirillin, I. Y. Lysenko, M. A. Turchaninov, and L. R. Fokin, Tech. Phys. Lett. **36**, 559 (2010).
[29]A. Y. Basharin, I. Y. Lysenko, and M. A. Turchaninov, High Temp. **50**, 464 (2012).
[30]B. C. Larson, J. Z. Tischler, and D. M. Mills, J. Mater. Res. **1**, 144 (2011).
[31]J. Z. Tischler, B. C. Larson, and D. M. Mills, Appl. Phys. Lett. **52**, 1785 (1988).
[32]S. L. Johnson, P. A. Heimann, A. G. MacPhee, A. M. Lindenberg, O. R. Monteiro, Z. Chang, R. W. Lee, and R. W. Falcone, Phys. Rev. Lett. **94**, 057407 (2005).
[33]C. J. Wu, J. N. Glosli, G. Galli, and F. H. Ree, Phys. Rev. Lett. **89**, 135701 (2002).
[34]J. Narayan and B. C. Larson, J. Appl. Phys. **93**, 278 (2003).
[35]J. Narayan and A. Bhaumik, "Direct Conversion of h-BN into pure c-BN at Ambient Temperatures and Pressures in Air," APL Mater. (in press).